

Supporting information

Biporous Metal–organic Framework with Tuneable CO₂/CH₄ Separation Performance Facilitated by Intrinsic Flexibility

Andrzej Gładysiak,^a Kathryn S. Deeg,^b Iurii Dovgaliuk,^c Arunraj Chidambaram,^a Kaili Ordiz,^d Peter G. Boyd,^a Seyed Mohamad Moosavi,^a Daniele Ongari,^a Jorge A. R. Navarro,^e Berend Smit^{a,b,d} and Kyriakos C. Stylianou*^a

^a Laboratory of Molecular Simulation (LSMO), Institut des sciences et ingénierie chimiques (ISIC), École polytechnique fédérale de Lausanne (EPFL) Valais, Rue de l'Industrie 17, 1951 Sion, Switzerland.

^b Department of Chemistry, University of California, Berkeley CA 94720, USA

^c Swiss-Norwegian Beamlines, European Synchrotron Radiation Facility, 38000 Grenoble, France

^d Department of Chemical and Biomolecular Engineering, University of California, Berkeley CA 94720, USA

^e Departamento de Química Inorgánica, Universidad de Granada, Av. Fuentenueva S/N, 18071 Granada, Spain

E-mail: kyriakos.stylianou@epfl.ch

Table S1. Crystal data and structure refinement for **SION-8** – CCDC: 1846814.

Identification code	SION-8
Empirical formula	C ₂₅ H ₂₀ CaO ₆ N
Formula weight	470.50
Temperature/K	100
Crystal system	orthorhombic
Space group	<i>Pbam</i>
<i>a</i> /Å	6.88590(11)
<i>b</i> /Å	20.0624(4)
<i>c</i> /Å	16.6453(4)
$\alpha/^\circ$	90
$\beta/^\circ$	90
$\gamma/^\circ$	90
Volume/Å ³	2299.51(8)
<i>Z</i>	4
$\rho_{\text{calc}} / \text{g/cm}^3$	1.359
μ/mm^{-1}	0.281
<i>F</i> (000)	980.0
Crystal size/mm ³	0.14 × 0.1 × 0.03
Radiation	synchrotron ($\lambda = 0.7153$)
2 Θ range for data collection/°	4.086 to 50.81
Index ranges	$-8 \leq h \leq 6, -23 \leq k \leq 23, -19 \leq l \leq 16$
Reflections collected	14679
Independent reflections	2064 [$R_{\text{int}} = 0.0294, R_{\text{sigma}} = 0.0140$]
Data/restraints/parameters	2064/82/170
Goodness-of-fit on <i>F</i> ²	1.916
Final R indexes [$I \geq 2\sigma(I)$]	$R_1 = 0.1024, wR_2 = 0.3739$
Final R indexes [all data]	$R_1 = 0.1053, wR_2 = 0.3805$
Largest diff. peak/hole / e Å ⁻³	2.23/-0.54

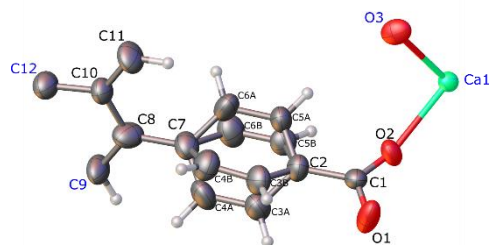


Figure S1. Asymmetric unit of **SION-8**. Atoms Ca1, O3, C9, and C12 (captioned in blue) are located at the special positions with the 0.5-occupancy, while atoms C3, C4, C5, and C6 are disordered over two distinct positions.

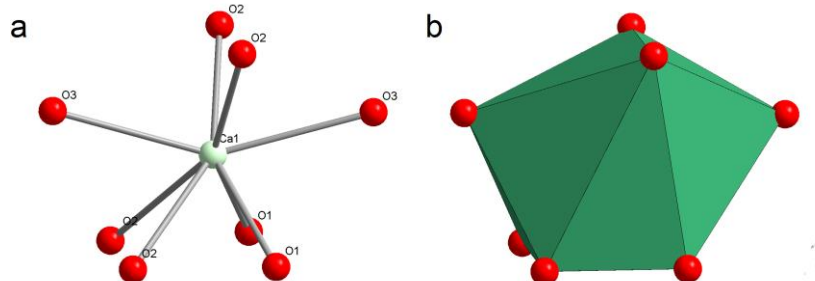


Figure S2. Coordination environment of the Ca1 atom in the structure of **SION-8**. (a) Atoms present in the first coordination shell of Ca1. (b) Coordination geometry described as biaugmented trigonal prism.

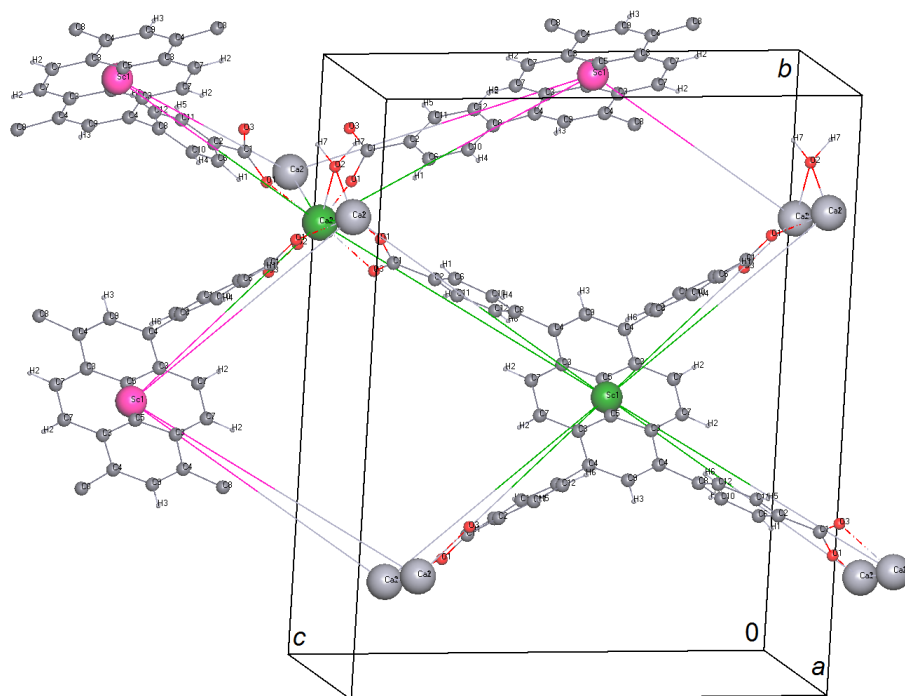


Figure S3. **SION-8** and its underlying *sea* net topology. The *sea* net is 2-nodal 6,8-coordinated with the $(6\text{-c})_2(8\text{-c})$ stoichiometry and Schläfli symbol $(3^4.4^{12}.5^4.6^8)(3^4.4^4.5^4.6^3)_2$. The 8-coordinated node marked as “Sc1” represents the center of the TBA Py^{4-} ligand. The Ca atom constitutes the 6-coordinated node connected to two neighboring Ca nodes and four imminent “Sc1” (TBAPy^{4-}) nodes. The full coordination of two selected nodes, one 8-c and one 6-c, marked in green, is depicted. The contour of the unit cell is outlined in black.

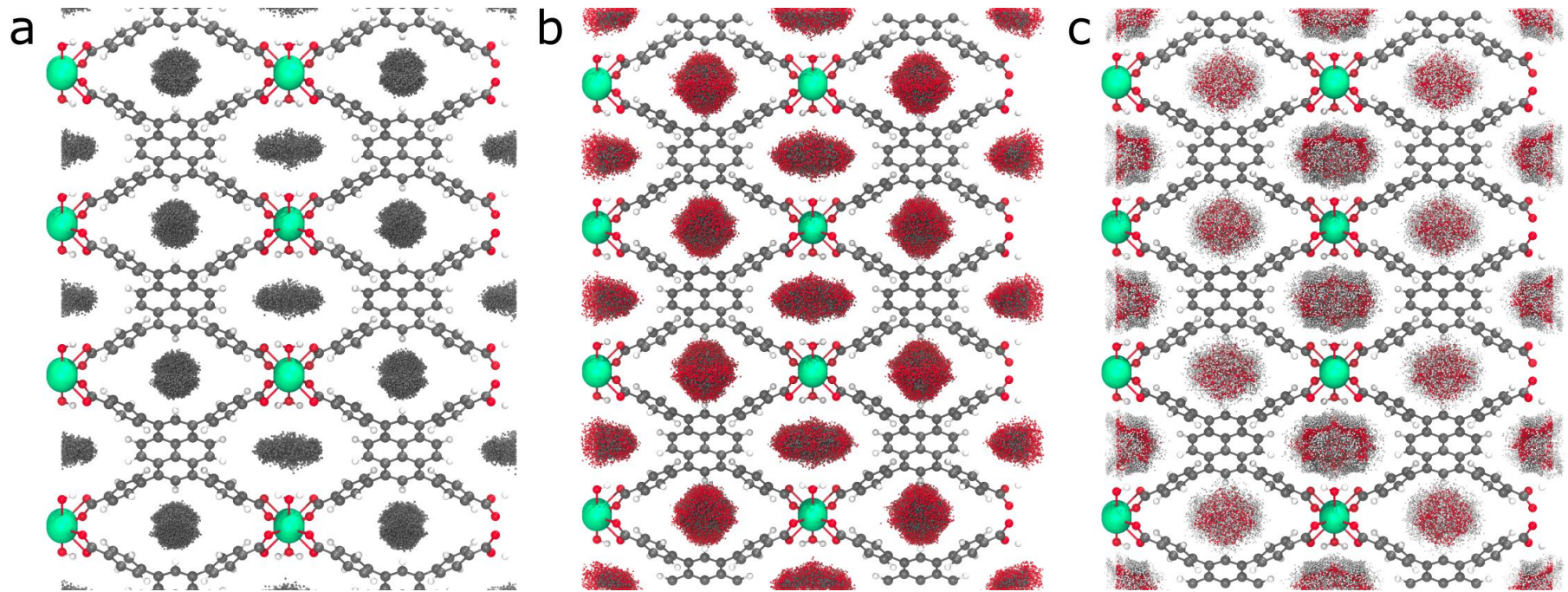


Figure S4. To visualize the positions of guest molecules and their affinity with the two different pores at zero loading, one guest molecule was inserted in the structure of **SION-8F**, letting it move according to the Monte Carlo NVT scheme at 293 K. The molecule is therefore allowed to jump from one pore to the other even though the two pores are not connected. Different snapshots of the trajectory were superimposed [(a) methane (united atom), (b) CO₂, and (c) water] and the number of molecules in each pore was counted for the entire simulation. In contrast to CO₂, water shows a structural rearrangement in the hydrophilic pore, with its hydrogen pointing to the carboxylic oxygens of the structure. Moreover, the higher affinity of the water to the hydrophilic pore is demonstrated by the atom count as measured from these simulations: 34.87%, 32.0% and 81.28% residence in the hydrophilic pore for CO₂, methane and water, respectively. In addition, the hydrophilic pore shows greater affinity ($-24(1)$ kJ/mol) for water at zero loading compared to the hydrophobic pore ($-14.90(2)$ kJ/mol).

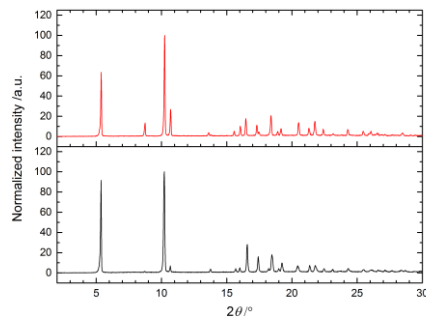


Figure S5. Powder pattern (recorded with Cu K α radiation) of **SION-8** before (top red plots) and after (bottom black plots) the immersion of the powder in pure H₂O for 24 h.

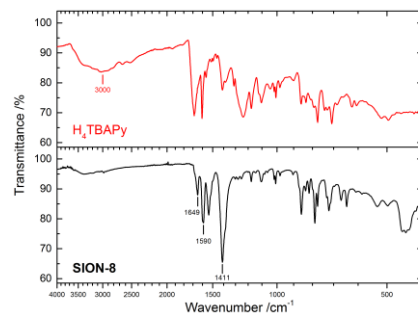


Figure S6. Infrared spectrum of **SION-8** (bottom black plots) compared to the spectrum of H₄TBAPy ligand (top red plots). Characteristic peaks mentioned in the Discussion are captioned.

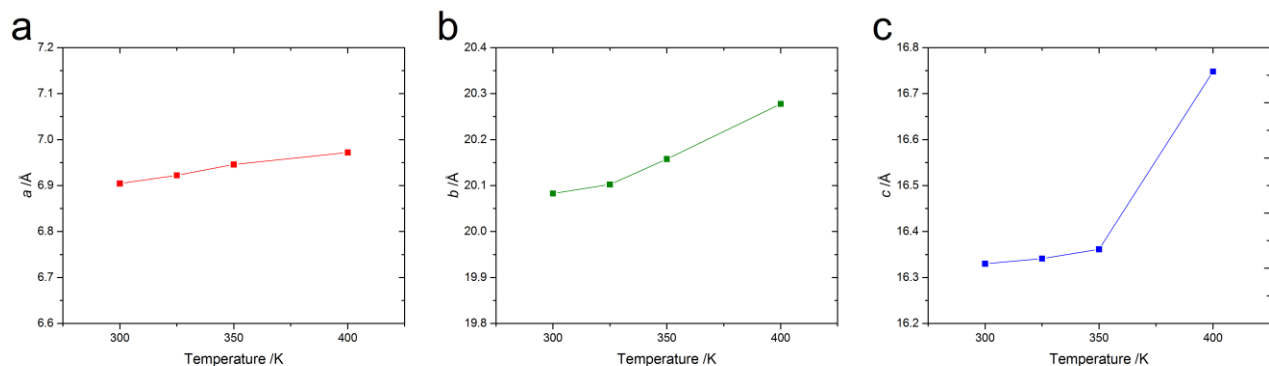


Figure S7. Parameters *a* (a), *b* (b), and *c* (c) of the orthorhombic unit cell of **SION-8** during its activation under vacuum plotted against temperature.

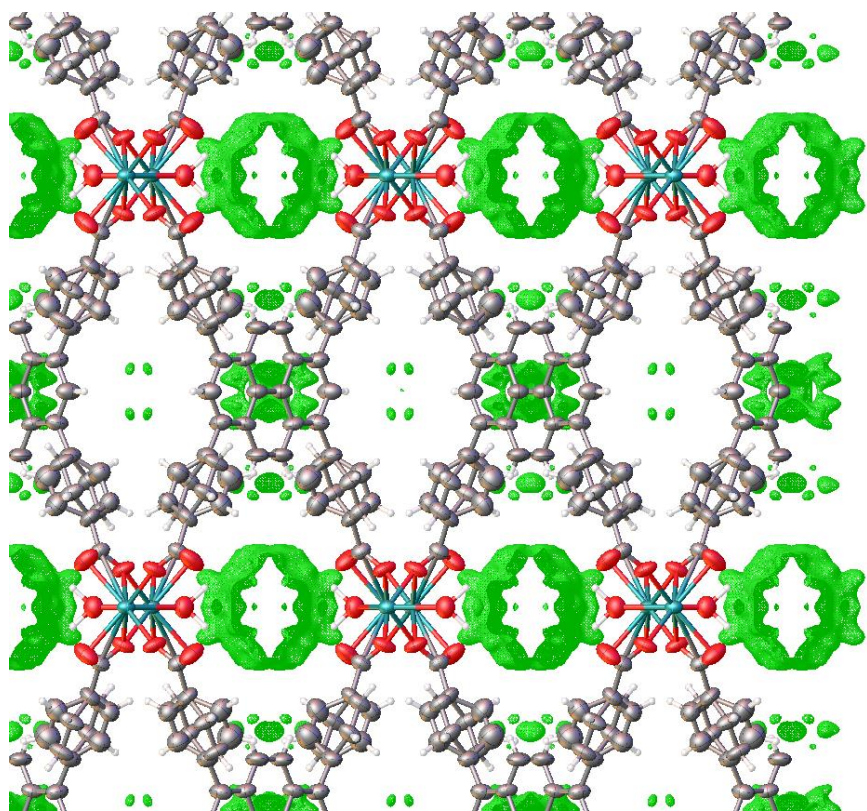


Figure S8. Difference–Fourier map of the crystal structure of **SION-8** at 400 K and under vacuum drawn with the program Olex2. The excess electron density map is represented in the wire style at the $0.5 \text{ e}^-/\text{\AA}^3$ level with the 0.1 \AA resolution. View along [100].

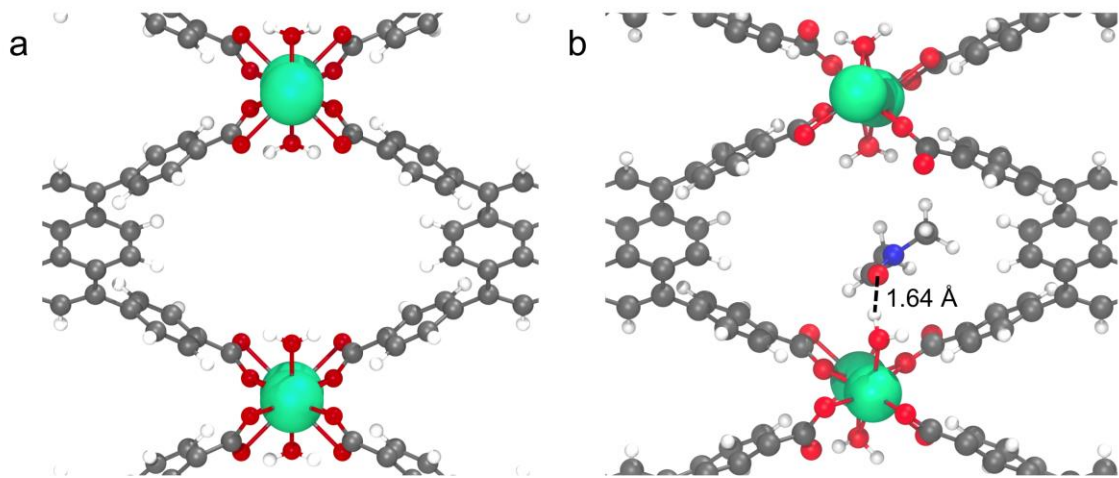


Figure S9. (a) Empty structure and (b) result of DFT relaxation of one DMF molecule in a hydrophilic pore of **SION-8**. Note that both the MOF and DMF atoms are allowed to move during the relaxation; this is necessary for the structural relaxation that facilitates hydrogen bonding between DMF and the coordinated water molecule.

$$C_{ij} = \begin{pmatrix} C_{11} & C_{12} & C_{13} & 0 & 0 & 0 \\ & C_{22} & C_{23} & 0 & 0 & 0 \\ & & C_{33} & 0 & 0 & 0 \\ & & & C_{44} & 0 & 0 \\ & & & & C_{55} & 0 \\ & & & & & C_{66} \end{pmatrix} = \begin{pmatrix} 15.3 & 2.3 & 8.3 & 0 & 0 & 0 \\ & 3.5 & 8.2 & 0 & 0 & 0 \\ & & 24.8 & 0 & 0 & 0 \\ & & & 1.8 & 0 & 0 \\ & & & & 1.8 & 0 \\ & & & & & 1.8 \end{pmatrix}$$

Scheme S1. The symmetric general stiffness tensor for an orthorhombic crystal and the DFT-computed elements of this tensor of **SION-8** expressed in GPa.

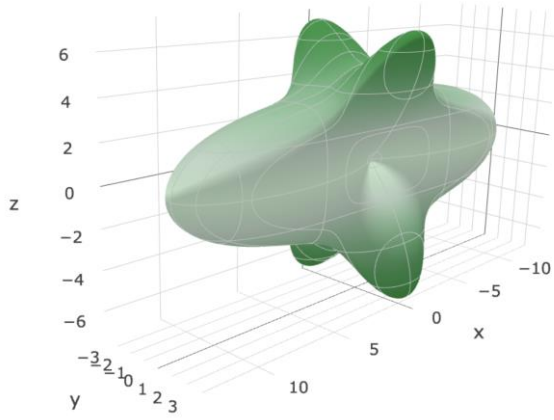


Figure S10. Side view of the 3-dimensional representation of Young's modulus of **SION-8**. Crystal's compliance along the *b*-axis (very low value of the Young's modulus, expressed in GPa, along the *y*-axis in the Cartesian coordinates) as well as crystal's stiffness along the *a*-axis and approximately along the [011] direction (respectively high values of the Young's modulus) are clearly appreciable.

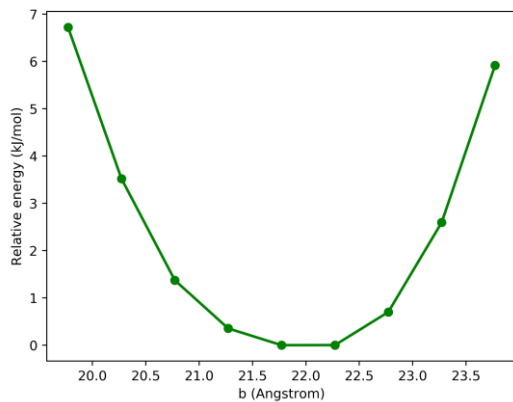


Figure S11. DFT-computed energy of **SION-8F** with different imposed values of the unit-cell parameter *b* while *a*, *c*, and the entire structure are allowed to relax, demonstrating the energy penalty of altering *b*.

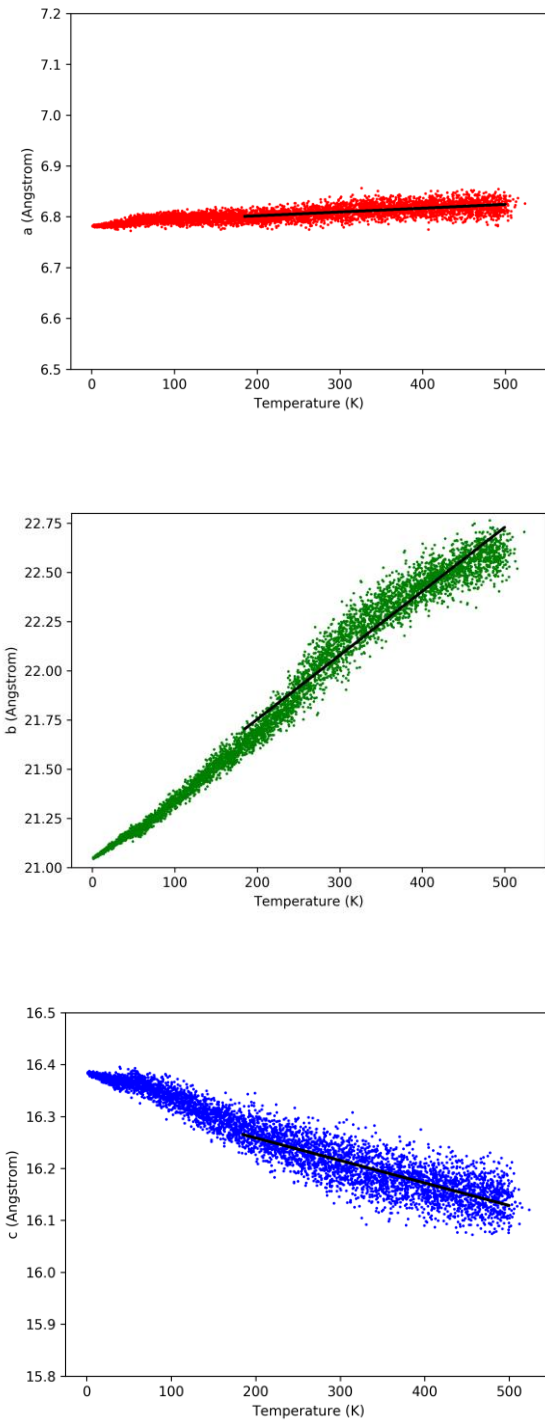


Figure S12. Temperature dependence of the unit-cell parameters a , b , and c , as computed from NPT Molecular Dynamics (MD) simulations. The UFF force field (Rappe *et al.*, 1992) was employed to describe the intermolecular potentials. The system was initialized at 500 K and a slow annealing was performed with a temperature ramp of -100 K per nanosecond. The a , b and c dimensions were recorded every picosecond (1000 MD steps). The average contraction of each dimension over temperature drop is shown as a linear fit between 500 K and 200 K.

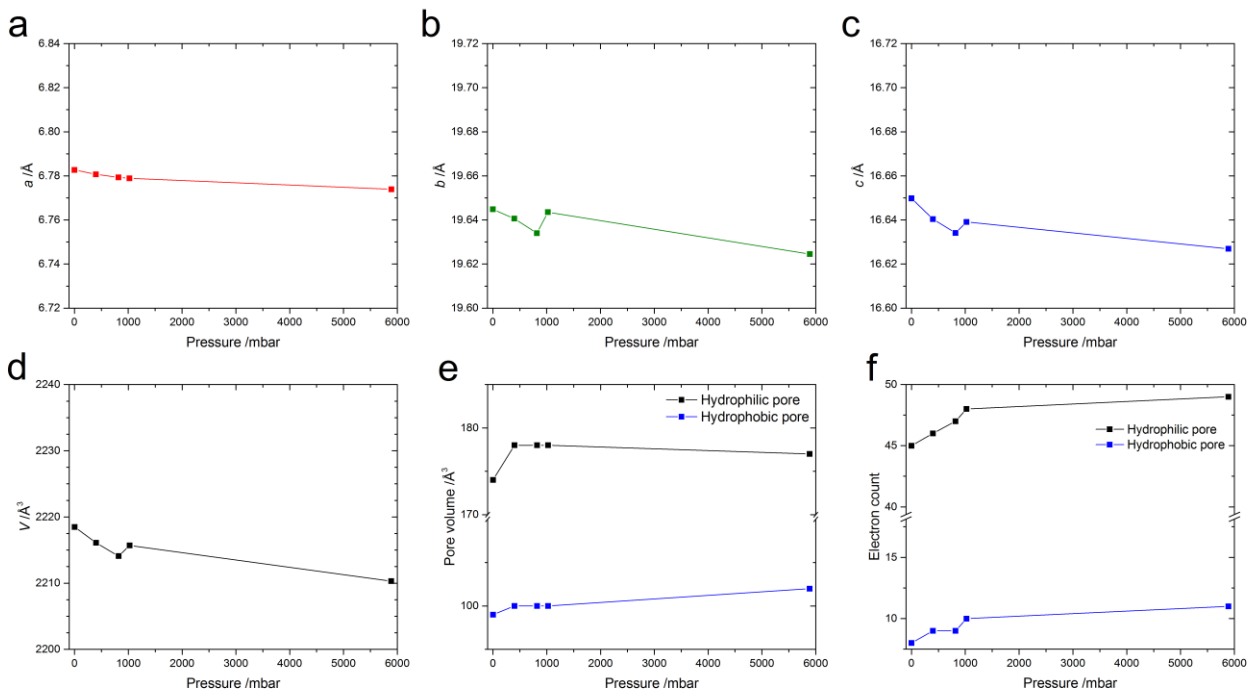


Figure S13. Structural parameters of SION-8 plotted against pressure of nitrogen. (a-d) Unit-cell parameters a , b , c and V . (e) Volume of hydrophilic (black plots) and hydrophobic (blue plots) pores as calculated with SQUEEZE. (f) Excess electron density per pore found in both types of pores. Isotherm measured at $T = 90$ K.

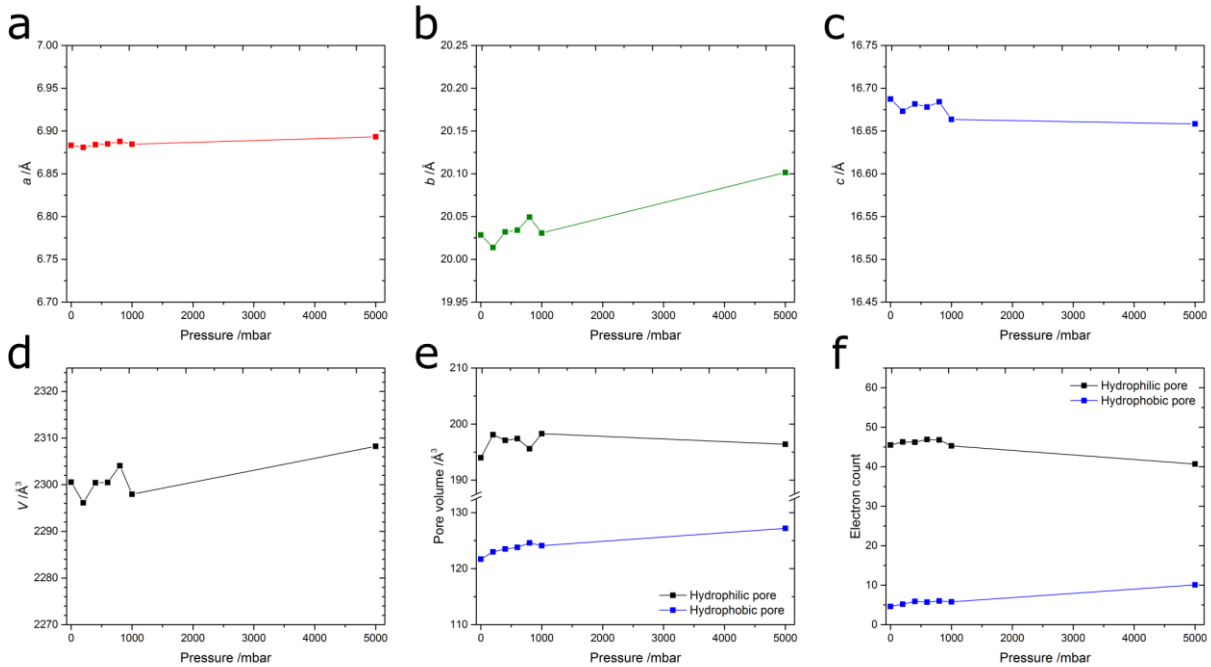


Figure S14. Structural parameters of SION-8 plotted against pressure of methane. (a-d) Unit-cell parameters a , b , c and V . (e) Volume of hydrophilic (black plots) and hydrophobic (blue plots) pores as calculated with SQUEEZE. (f) Excess electron density per pore found in both types of pores. Isotherm measured at $T = 300$ K.

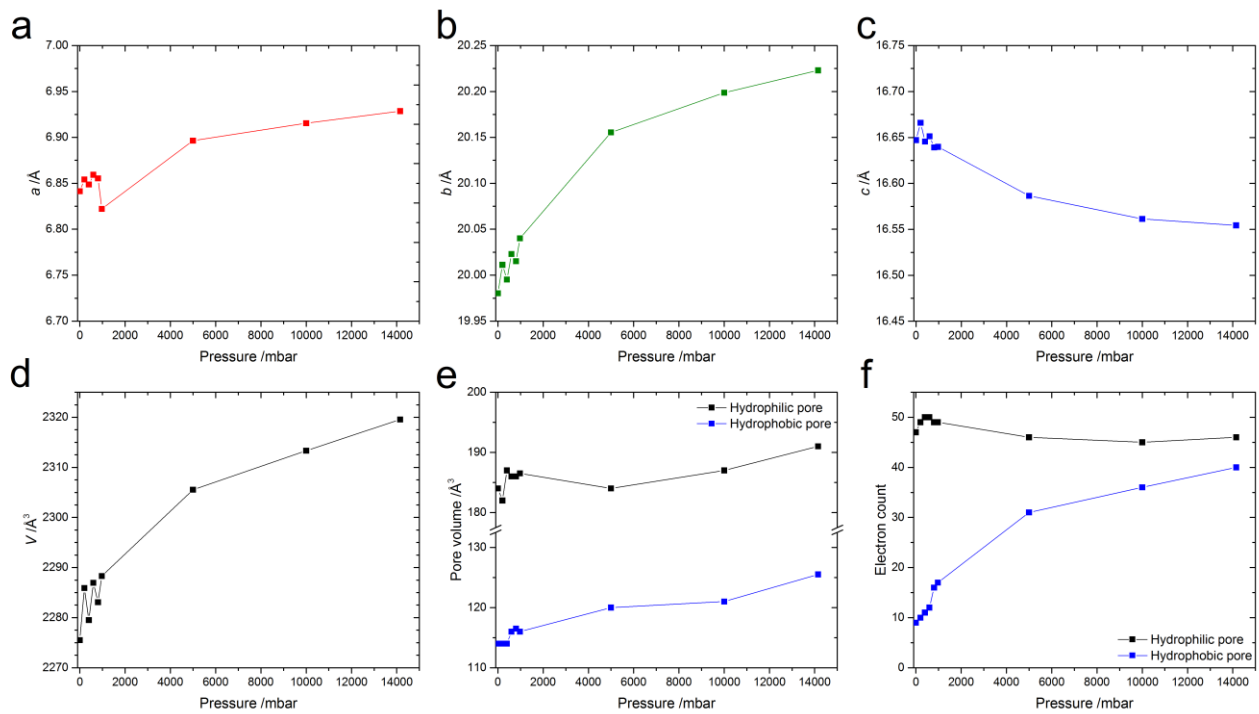


Figure S15. Structural parameters of SION-8 plotted against pressure of carbon dioxide. (a-d) Unit-cell parameters a , b , c and V . (e) Volume of hydrophilic (black plots) and hydrophobic (blue plots) pores as calculated with SQUEEZE. (f) Excess electron density per pore found in both types of pores. Isotherm measured at $T = 300$ K.

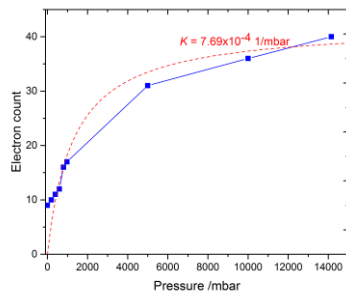


Figure S16. Excess electron density found in the hydrophobic pore plotted against the pressure of CO_2 (blue plots) fitted to the Langmuir model (dashed red line).

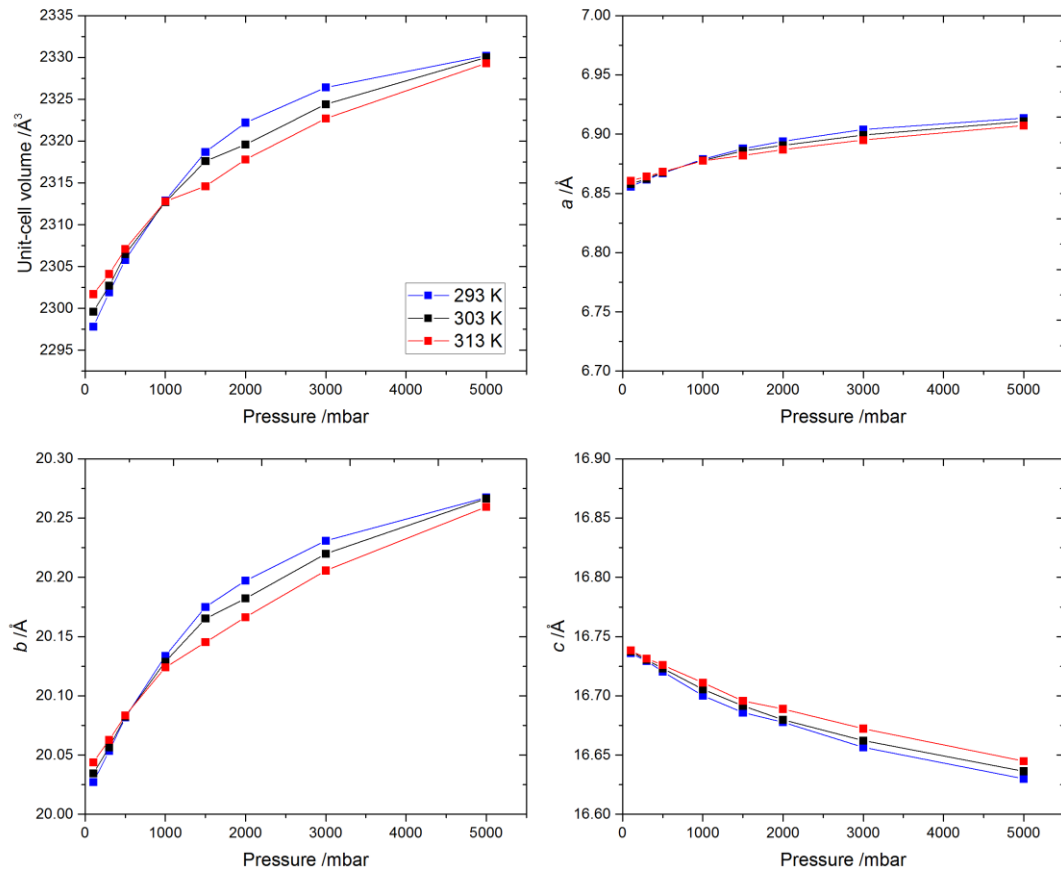


Figure S17. Unit-cell volume and parameters a , b , and c of **SION-8F** derived from the Le Bail fits to the PXRD patterns recorded during the *in-situ* CO_2 -loading experiment ($\lambda = 0.72179 \text{ \AA}$).

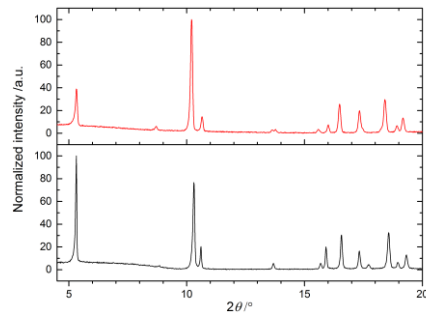


Figure S18. Powder pattern (recorded with $\text{Cu K}\alpha$ radiation) of a sample of **SION-8** before (top red plots) and after (bottom black plots) the adsorption experiment. No loss in crystallinity is clearly visible.

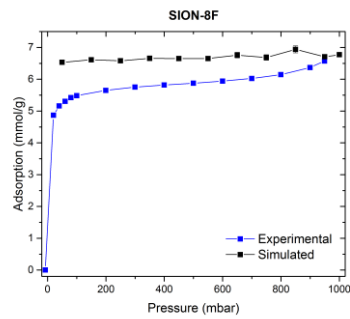


Figure S19. Simulated N₂-adsorption isotherm in **SION-8F** (black plots) compared to the experimental one (blue plots).

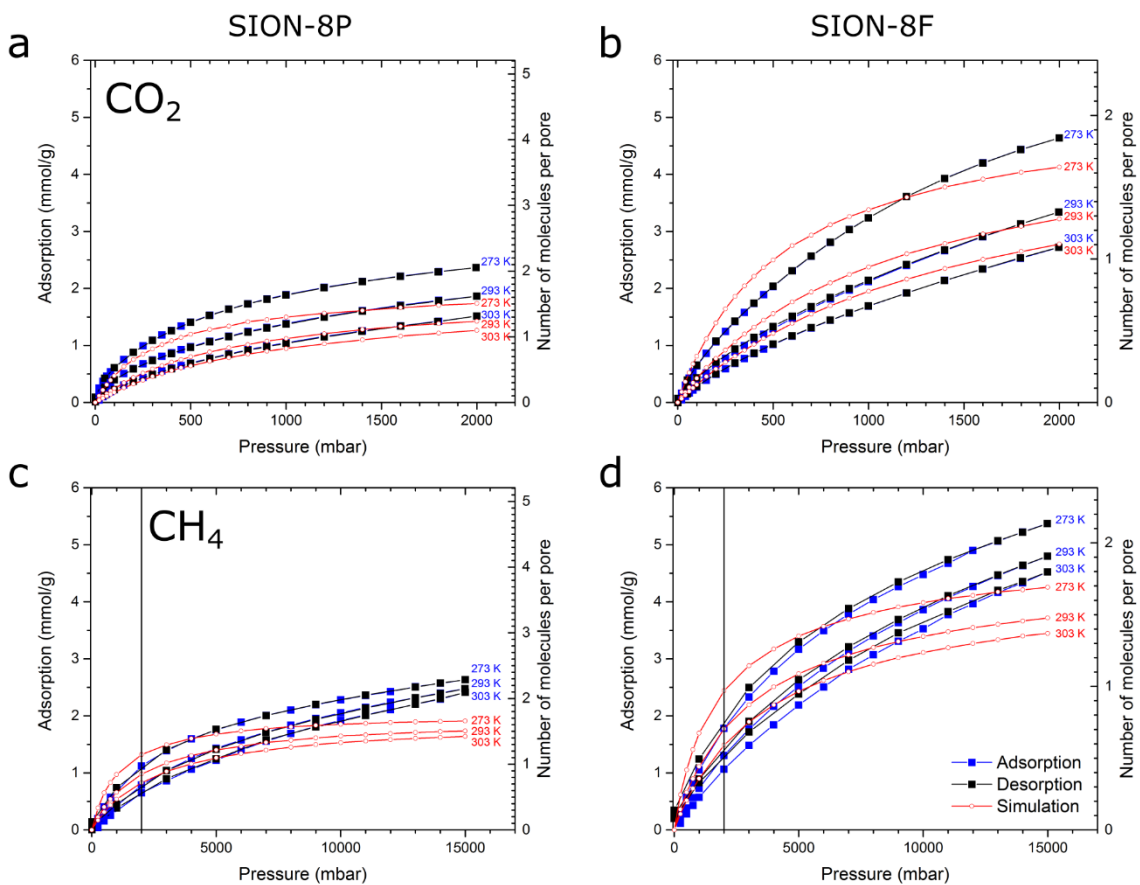


Figure S20. Comparison between the experimental and simulated adsorption isotherms at 273 K, 293 K and 303 K: (a) CO₂ adsorption isotherms for **SION-8P**. (b) CO₂ adsorption isotherms for **SION-8F**. (c) CH₄ adsorption isotherms for **SION-8P**. (d) CH₄ adsorption isotherms for **SION-8F**.

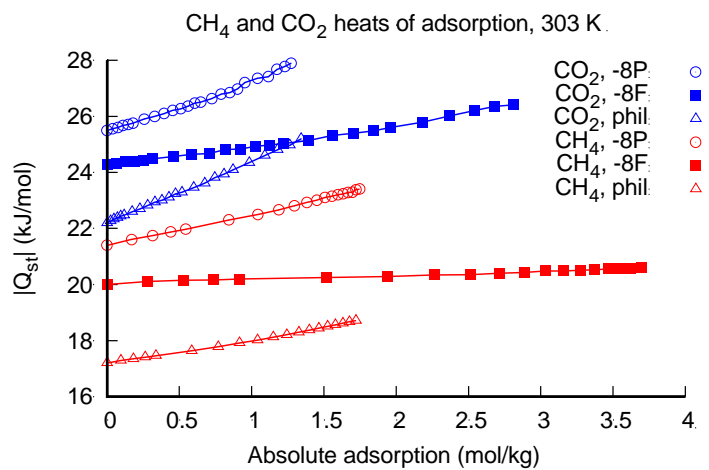
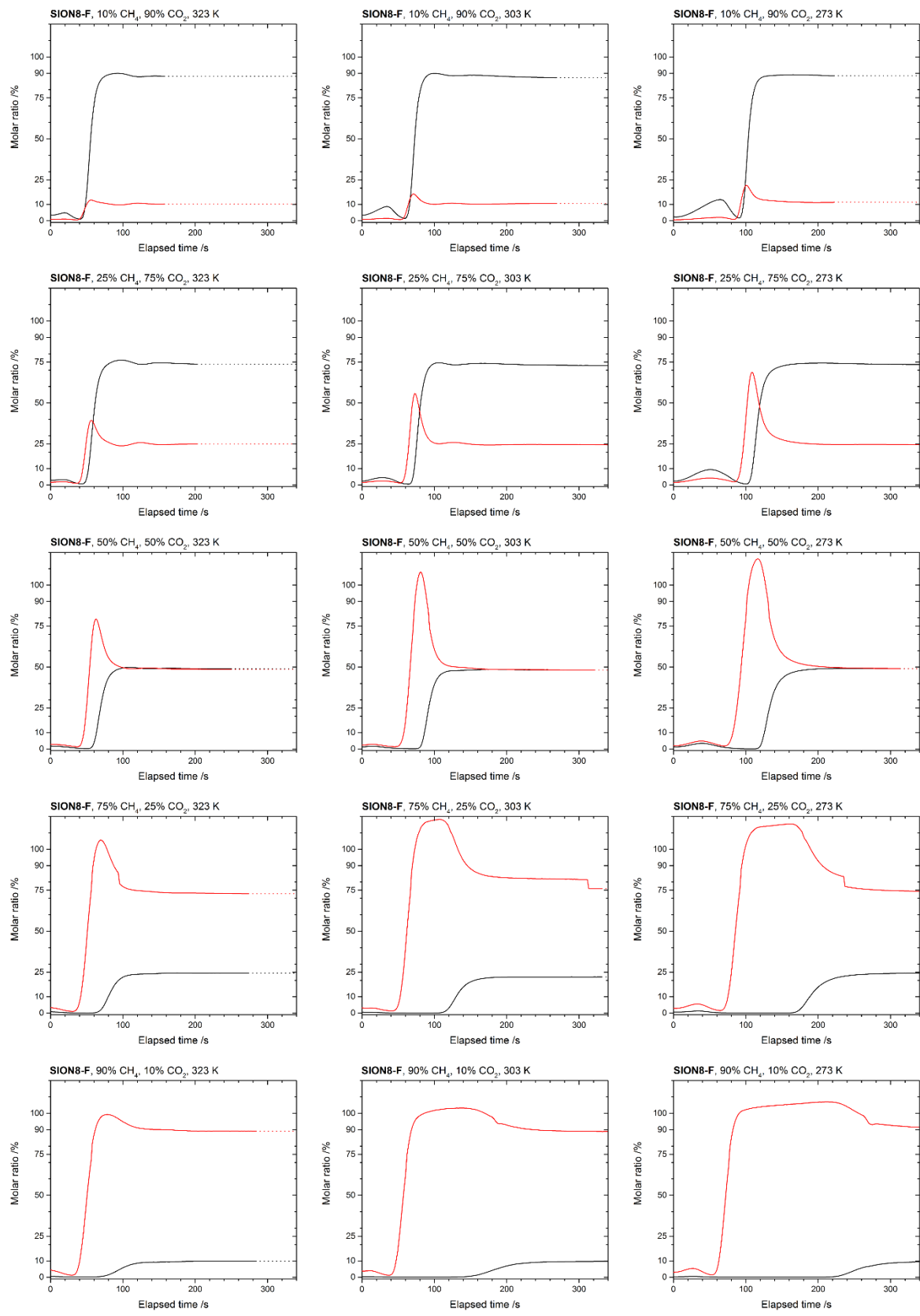


Figure S21. Heats of adsorption of CH₄ and CO₂ as computed from GCMC simulations (except those at zero loading, which were computed from Widom insertions). Loadings correspond to those considered in the adsorption isotherms. “-8P” refers to adsorption in **SION-8P**, “-8F” refers to adsorption in **SION-8F**, and “phil” refers to adsorption in the hypothetical **SION-8** with only the hydrophilic pore available for guest adsorption.



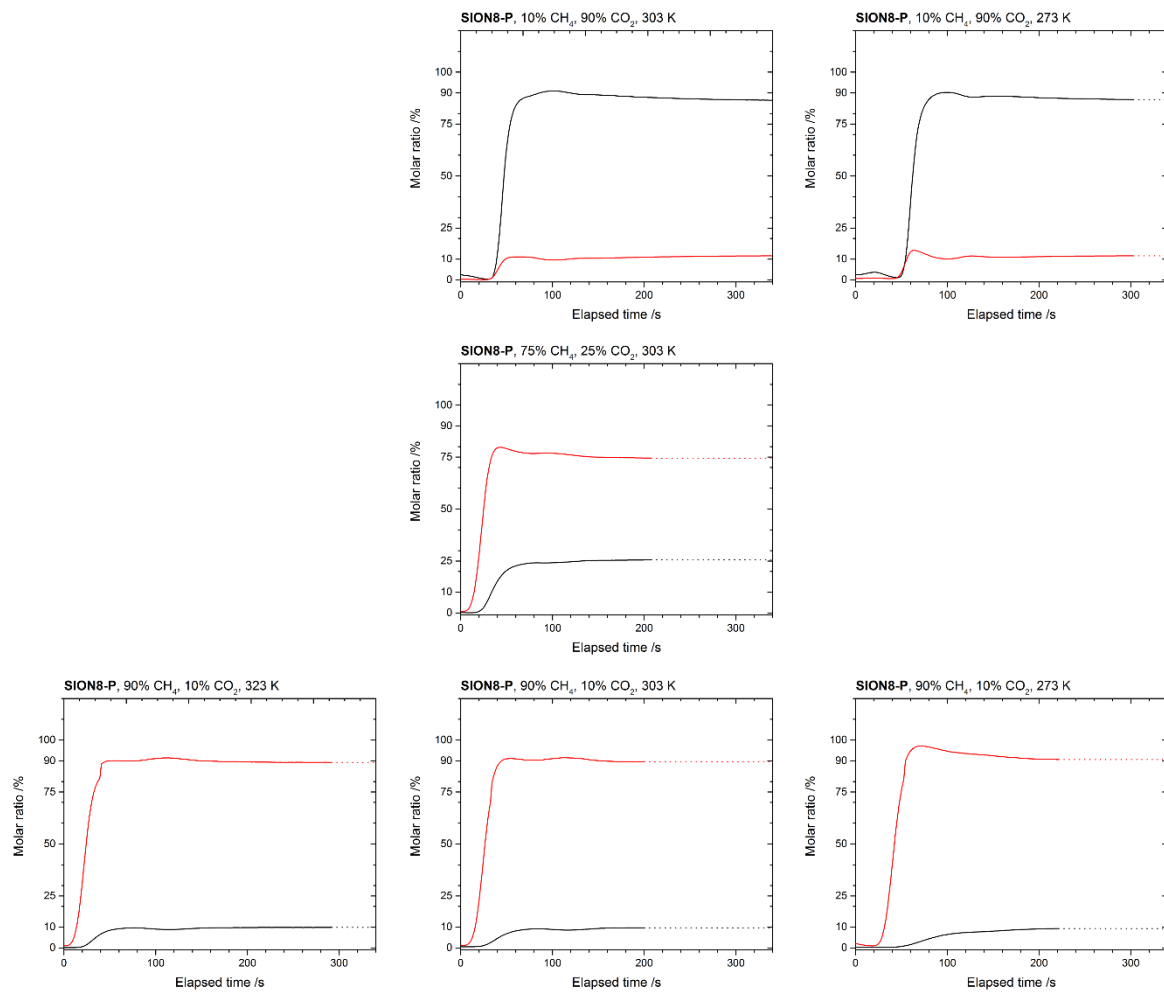


Figure S22. Breakthrough curves for **SION-8F** and **SION-8P** recorded at 273 K, 303 K and 323 K, and at different compositions of CO₂/CH₄ gas mixtures. Color code: CO₂; black, CH₄; red.

Table S2. Adsorption capacities of **SION-8P** and **SION-8F** calculated by integrating breakthrough curves. Values in mmol/g.

SION-8F

	10% CH ₄ , 90% CO ₂		25% CH ₄ , 75% CO ₂		50% CH ₄ , 50% CO ₂		75% CH ₄ , 25% CO ₂		90% CH ₄ , 10% CO ₂	
	CO ₂	CH ₄								
273 K	1.92	0.10	1.89	0.29	1.46	0.47	1.08	0.60	0.56	0.92
303 K	1.38	0.09	1.35	0.26	0.98	0.56	0.64	0.61	0.37	0.90
323 K	1.00	0.07	0.88	0.19	0.69	0.43	0.43	0.67	0.19	0.88

SION-8P

	10% CH ₄ , 90% CO ₂		25% CH ₄ , 75% CO ₂		50% CH ₄ , 50% CO ₂		75% CH ₄ , 25% CO ₂		90% CH ₄ , 10% CO ₂	
	CO ₂	CH ₄								
273 K	1.57	0.16							0.30	1.29
303 K	1.11	0.12					0.39	0.83	0.18	1.13
323 K									0.16	1.03

Table S3. MOFs exhibiting the CO₂/CH₄ separation performance determined with breakthrough experiments reported in the literature.

Material	CO ₂ /CH ₄ feed ratio	Temp. [K]	Pressure [bar]	CO ₂ capacity [mmol/g]	CH ₄ capacity [mmol/g]	CO ₂ /CH ₄ dynamic selectivity	Reference
Al-BDC calcinated	0.50/0.50	303	1			10.5	Sun <i>et al.</i> , 2014
Al-BDC calcinated	0.50/0.50	303	2			12.3	Sun <i>et al.</i> , 2014
CCP-1	0.50/0.50	298	2			2	Giménez-Marqués <i>et al.</i> , 2017
CPO-27-Ni	0.50/0.50	303	1			15	García <i>et al.</i> , 2012
CPO-27-Co	0.50/0.50	303	1			12	García <i>et al.</i> , 2012
CPO-27-Zn	0.50/0.50	303	1			9	García <i>et al.</i> , 2012
Cu-BTC	0.25/0.75	303	1	1.2	0.6	6.6	Hamon <i>et al.</i> , 2010
Cu-BTC	0.50/0.50	303	1	2.0	0.4	5.6	Hamon <i>et al.</i> , 2010
Cu-BTC	0.75/0.25	303	1	3.0	0.2	6.6	Hamon <i>et al.</i> , 2010
Mg-MOF-74	0.20/0.80			2.02	≈0	close to infinite	Britt <i>et al.</i> , 2009
MIL-100(Fe)	0.50/0.50	303		1.49	0.28	5.3	Xian <i>et al.</i> , 2015
MIL-100(Fe), 50% RH	0.50/0.50	303		3.75	0.23	16.3	Xian <i>et al.</i> , 2015
MIL-100(Fe)	0.20/0.80	303		0.87	1.21	2.9	Xian <i>et al.</i> , 2015
MIL-101(Cr)	0.50/0.50	303		2.44	0.54	4.5	Xian <i>et al.</i> , 2015
MIL-101(Cr), 50% RH	0.50/0.50	303		1.37	0.37	3.7	Xian <i>et al.</i> , 2015
MIL-101(Cr)	0.15/0.85	303		1.67	1.80	3.7	Xian <i>et al.</i> , 2015
MIL-101(Al)-NH ₂	0.15/0.85	298	1	0.8		66.3	Serra-Crespo <i>et al.</i> , 2011
MIL-101(Al)-NH ₂	0.30/0.70	298	1	1.0		34.7	Serra-Crespo <i>et al.</i> , 2011
MIL-101(Al)-NH ₂	0.40/0.60	298	1	1.1		14.2	Serra-Crespo <i>et al.</i> , 2011
MIL-101(Al)-NH ₂	0.50/0.50	298	1	1.2		6.3	Serra-Crespo <i>et al.</i> , 2011
MIL-101(Cr)	0.30/0.70	298	1			7.5	Serra-Crespo <i>et al.</i> , 2011
MIL-101(Cr)	0.50/0.50	298	1			3.6	Serra-Crespo <i>et al.</i> , 2011
MIL-53(Al)-NH ₂	0.50/0.50	303	1	0.83	≈0	“almost infinite”	Couck <i>et al.</i> , 2009; revised by Couck <i>et al.</i> , 2012
MIL-53(Al)-NH ₂	0.90/0.10	303	1			59	Couck <i>et al.</i> , 2012
MIL-53(Al)-NH ₂	0.70/0.30	303	1			23	Couck <i>et al.</i> , 2012
MIL-53(Al)-NH ₂	0.50/0.50	303	1	1.3	0.04	45	Couck <i>et al.</i> , 2012
MIL-53(Al)-NH ₂	0.30/0.70	303	1			90	Couck <i>et al.</i> , 2012
MIL-53(Al)-NH ₂	0.10/0.90	303	1			213	Couck <i>et al.</i> , 2012
MIL-53(Al,PVA)	0.50/0.50	303	1	1.3	0.2	7	Finsy <i>et al.</i> , 2009
MIL-53(Al,PVA)	0.25/0.75	303	1	0.65	0.5	3.9	Finsy <i>et al.</i> , 2009
MIL-53(Al,PVA)	0.47/0.53	303	1	1.3	0.25	6.6	Finsy <i>et al.</i> , 2009
MIL-53(Al,PVA)	0.75/0.25	303	1	1.5	0.08	6.2	Finsy <i>et al.</i> , 2009
MIL-53(Cr)	0.25/0.75	303	1			13	Hamon <i>et al.</i> , 2009
MOF-508b	0.50/0.50	303	1	0.19	0.17	3	Bastin <i>et al.</i> , 2008
SIFSIX-2-Cu-i	0.50/0.50	298	1		3.14	51	Nugent <i>et al.</i> , 2013
STA-12-Ni	0.50/0.50	303	1			6	García <i>et al.</i> , 2012
α-[Zn(bcba)]	0.10/0.90	298	1	0.35	0.11	2.9	Huang <i>et al.</i> , 2018
α-[Zn(bcba)]	0.40/0.60	298	1	0.25	0.38	2.3	Huang <i>et al.</i> , 2018
β-[Zn(bcba)]	0.10/0.90	298	1	0.15	0.50	32	Huang <i>et al.</i> , 2018

β -[Zn(bcba)]	0.40/0.60	298	1	0.07	1.20	29	Huang <i>et al.</i> , 2018
ZJNU-54	0.50/0.50	298	1.01	2.19		5.2	Jiao <i>et al.</i> , 2016

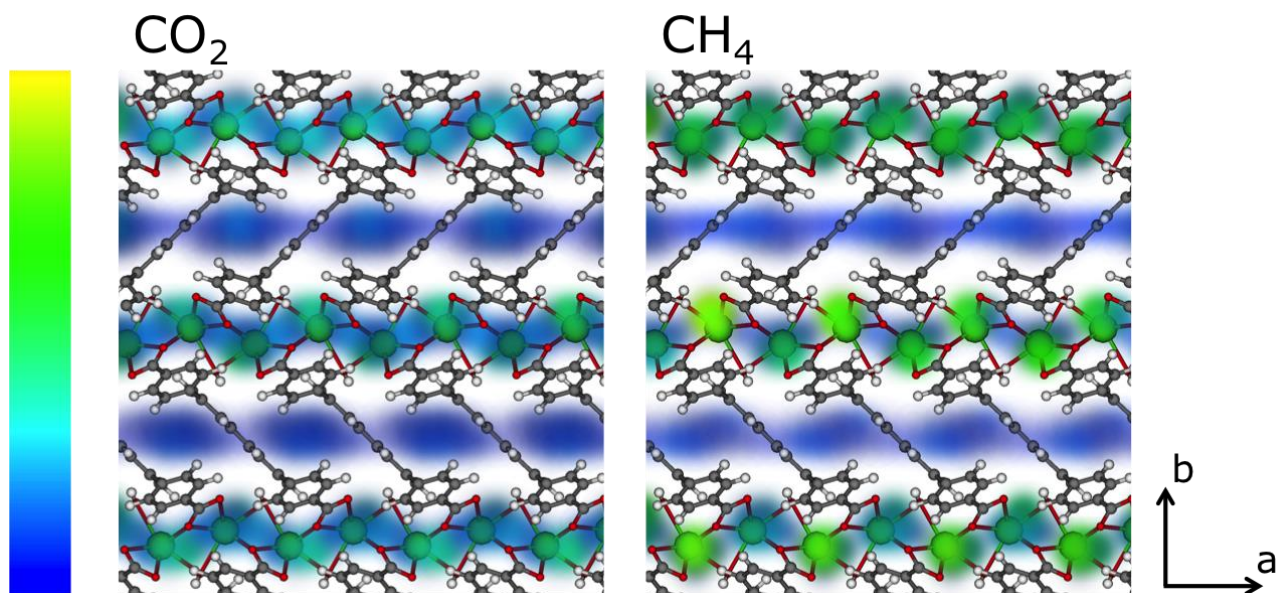


Figure S23. Alternate view of probability density plots of adsorbate positions in **SION-8F**, generated from Monte Carlo NVT simulations with 2 molecules per unit cell, at 293 K. The color bar on the left denotes low (blue) to high (yellow) relative probability.

References

- Bastin, L.; Bárcia, P. S.; Hurtado, E. J.; Silva, J. A. C.; Rodrigues, A. E.; Chen, B. A Microporous Metal–Organic Framework for Separation of CO₂/N₂ and CO₂/CH₄ by Fixed-Bed Adsorption. *J. Phys. Chem. C* **2008**, *112*, 1575–1581.
- Britt, D.; Furukawa, H.; Wang, B.; Glover, T. G.; Yaghi, O. M. Highly Efficient Separation of Carbon Dioxide by a Metal–organic Framework Replete with Open Metal Sites. *Proc. Natl. Acad. Sci. U. S. A.* **2009**, *106*, 20637–20640.
- Couck, S.; Denayer, J. F. M.; Baron, G. V.; Rémy, T.; Gascon, J.; Kapteijn, F. An Amine-Functionalized MIL-53 Metal–Organic Framework with Large Separation Power for CO₂ and CH₄. *J. Am. Chem. Soc.* **2009**, *131*, 6326–6327.
- Couck, S.; Gobechiya, E.; Kirschhock, C. E. A.; Serra-Crespo, P.; Juan-Alcañiz, J.; Joaristi, A. M.; Stavitski, E.; Gascon, J.; Kapteijn, F.; Baron, G. V.; Denayer, J. F. M. Adsorption and Separation of Light Gases on an Amino-Functionalized Metal–Organic Framework: An Adsorption and In Situ XRD Study. *ChemSusChem* **2012**, *5*, 740–750.
- Finsy, V.; Ma, L.; Alaerts, L.; De Vos, D. E.; Baron, G. V.; Denayer, J. F. M. Separation of CO₂/CH₄ Mixtures with the MIL-53(Al) Metal–organic Framework. *Micropor. Mesopor. Mater.* **2009**, *120*, 221–227.
- García, E. J.; Mowat, J. P. S.; Wright, P. A.; Pérez-Pellitero, J.; Jallut, C.; Pirngruber, G. D. Role of Structure and Chemistry in Controlling Separations of CO₂/CH₄ and CO₂/CH₄/CO Mixtures over Honeycomb MOFs with Coordinatively Unsaturated Metal Sites. *J. Phys. Chem. C* **2012**, *116*, 26636–26648.
- Giménez-Marques, M.; Calvo Galve, N.; Palomino, M.; Valencia, S.; Rey, F.; Sastre, G.; Vitorica-Yrezábal, I. J.; Jiménez-Ruiz, M.; Rodríguez-Velamazán, J. A.; González, M. A.; Jordá, J. L.; Coronado, E.; Espallargas, G. M. Gas Confinement in Compartmentalized Coordination Polymers for Highly Selective Sorption. *Chem. Sci.* **2017**, *8*, 3109–3120.
- Hamon, L.; Llewellyn, P. L.; Devic, T.; Ghoufi, A.; Clet, G.; Guillerm, V.; Pirngruber, G. D.; Maurin, G.; Serre, C.; Driver, G.; van Beek, W.; Jolimaître, E.; Vimont, A.; Daturi, M.; Férey, G. Co-adsorption and Separation of CO₂–CH₄ Mixtures in the Highly Flexible MIL-53(Cr) MOF. *J. Am. Chem. Soc.* **2009**, *131*, 17490–17499.
- Hamon, L.; Jolimaître, E.; Pirngruber, G. D. CO₂ and CH₄ Separation by Adsorption Using Cu-BTC Metal–Organic Framework. *Ind. Eng. Chem. Res.* **2010**, *49*, 7497–7503.
- Huang, N.-Y.; Mo, Z.-W.; Li, L.-J.; Xu, W.-J.; Zhou, H.-L.; Zhou, D.-D.; Liao, P.-Q.; Zhang, J.-P.; Chen, X.-M. Direct Synthesis of an Aliphatic Amine Functionalized Metal-organic Framework for Efficient CO₂ Removal and CH₄ Purification. *CrystEngComm* **2018**, doi: 10.1039/C8CE00574E.
- Jiao, J.; Dou, L.; Liu, H.; Chen, F.; Bai, D.; Feng, Y.; Xiong, S.; Chen, D. L.; He, Y. An Aminopyrimidine-functionalized Cage-based Metal–organic Framework Exhibiting Highly Selective Adsorption of C₂H₂ and CO₂ over CH₄. *Dalton Trans.* **2016**, *45*, 13373–13382.
- Nugent, P.; Belmabkhout, Y.; Burd, S. D.; Cairns, A. J.; Luebke, R.; Forrest, K.; Pham, T.; Ma, S.; Space, B.; Wojtas, L.; Eddaoudi, M.; Zaworotko, M. J. Porous Materials with Optimal Adsorption Thermodynamics and Kinetics for CO₂ Separation. *Nature* **2013**, *495*, 80–84.
- Rappe, A. K.; Casewit, C. J.; Colwell, K. S.; Goddard, W. A.; Skiff, W. M. UFF, a Full Periodic Table Force Field for Molecular Mechanics and Molecular Dynamics Simulations. *J. Am. Chem. Soc.* **1992**, *114*, 10024–10035.
- Serra-Crespo, P.; Ramos-Fernandez, E. V.; Gascon, J.; Kapteijn, F. Synthesis and Characterization of an Amino Functionalized MIL-101(Al): Separation and Catalytic Properties. *Chem. Mater.* **2011**, *23*, 2565–2572.
- Sun, T.; Hu, J.; Ren, X.; Wang, S. Experimental Evaluation of the Adsorption, Diffusion, and Separation of CH₄/N₂ and CH₄/CO₂ Mixtures on Al-BDC MOF. *Separ. Sci. Technol.* **2015**, *50*, 874–885.
- Xian, S.; Peng, J.; Zhang, Z.; Xia, Q.; Wang, H.; Li, Z. Highly Enhanced and Weakened Adsorption Properties of Two MOFs by Water Vapor for Separation of CO₂/CH₄ and CO₂/N₂ Binary Mixtures. *Chem. Eng. J.* **2015**, *270*, 385–392.